Magnet System for the Quantum Electromechanical Metrology Suite

Rafael R. Marangoni, Darine Haddad, *Member, IEEE*, Frank Seifert, Leon S. Chao, David B. Newell, and Stephan Schlamminger, *Member, IEEE*

***Abstract*— The design of the permanent magnet system for the new quantum electromechanical metrology suite (QEMMS) is described. The QEMMS, developed at the National Institute of Standards and Technology (NIST), consists of a Kibble balance, a programmable Josephson voltage standard, and a quantum Hall resistance standard. It will be used to measure masses up to 100 g with relative uncertainties below 2×10^{-8}. The magnet system is based on the design of the NIST-4 magnet system with significant changes to adopt to a smaller Kibble balance and to overcome known practical limitations. Analytical models are provided to describe the coil-current effect and model the forces required to split the magnet into two parts to install the coil. Both models are compared to simulation results obtained with finite-element analysis and measurement results. Other aspects such as the coil design and flatness of Bl profile are considered.**

***Index Terms*— Kibble balance, magnet circuit, magnet system, mass measurement.**

I. Introduction

THE Fundamental Electrical Measurements Group of the National Institute of Standards and Technology (NIST) is developing the quantum electromechanical metrology suite (QEMMS). This suite is a quantum metrology solution composed of a Kibble balance, a programmable Josephson voltage standard, and a quantum Hall resistance standard. The Kibble balance is being designed for measuring masses of 100 g with relative uncertainties lower than 2×10^{-8}. Since the revision of the International System of Units (SI) on 20 May, 2019, the definition of the kilogram unit is based on the Planck constant h and the definitions of the meter and second via fixed values of the speed of light and the unperturbed ground-state hyperfine transition frequency of Cesium-133, respectively. The Kibble balance provides one way to realize the unit of mass at the kilogram level with high accuracy.

In a Kibble balance, the weight of a mass m in a region with the acceleration of free fall g is compensated by the electromagnetic force of an electric current I in a magnetic field with flux density B. The electric current flows in a multiturn coil with length l. The high accuracy of the mass measurement can be achieved by precisely measuring g, I, and the product Bl during balance operation. The acceleration of free fall is measured with an absolute gravimeter, the electric current is measured by using a reference resistor in combination with a voltmeter, and the product Bl is measured by moving the coil in the magnetic field and determining the ratio between induced voltage and velocity. With the Kibble balance, it is theoretically possible to calibrate the standards of any mass value directly. This is an advantage for masses lower than 1 kg, which can be measured with lower uncertainties by reducing the metrological traceability chain [1].

The magnet system of a Kibble balance is responsible for generating the magnetic field with flux density B. Usually, a magnetic circuit with permanent magnets in an axially symmetric configuration is used to generate the magnetic field. The field must be stable in time and have a uniform profile along the travel range of the coil. It is advantageous to have a magnetic flux density with the highest possible magnitude. The requirements and design aspects of the magnet system of the QEMMS are described in this article.

II. Description of the System

The idea of the QEMMS Kibble balance is to realize the kilogram unit for masses up to 100 g with relative uncertainties smaller than 2×10^{-8} and as few operational requirements as possible. When compared to the NIST-4, the QEMMS will be smaller, simpler to operate, and easier to maintain. These principles will be used in the design of the balance components, including the magnet system.

Several requirements for the magnet system were defined prior to the design based on experiences gained with NIST-4 and Kibble balances at other laboratories: 1) the precision air gap should have a height of 4 cm; 2) the maximum relative deviation of the radial flux density in the precision air gap should be below 1×10^{-4}; and 3) the temperature coefficient of the flux density should be $1 \times 10^{-5}\ \mathrm{K}^{-1}$ or smaller. While the allowed variation of the flux density of the field in the precision gap is similar to that of NIST-4, the precision air gap height is two times and the temperature sensitivity 33 times smaller than the corresponding parameter of the magnet system used for the NIST-4 [3].

As described in [2], there are basically five possibilities for generating the magnetic flux density B: conventional electromagnets, superconducting magnets, permanent magnets with

Manuscript received August 15, 2019; revised November 1, 2019; accepted December 6, 2019. Date of publication December 16, 2019; date of current version June 24, 2020. The Associate Editor coordinating the review process was Tae-Weon Kang. *(Corresponding author: Rafael R. Marangoni.)*

R. R. Marangoni, D. Haddad, L. S. Chao, D. B. Newell, and S. Schlamminger are with the National Institute of Standards and Technology, Gaithersburg, MD 20899 USA (e-mail: rafael.marangoni@nist.gov).

F. Seifert is with the National Institute of Standards and Technology, Gaithersburg, MD 20899 USA, and also with the Joint Quantum Institute, University of Maryland at College Park, College Park, MD 20742 USA.

Digital Object Identifier 10.1109/TIM.2019.2959852

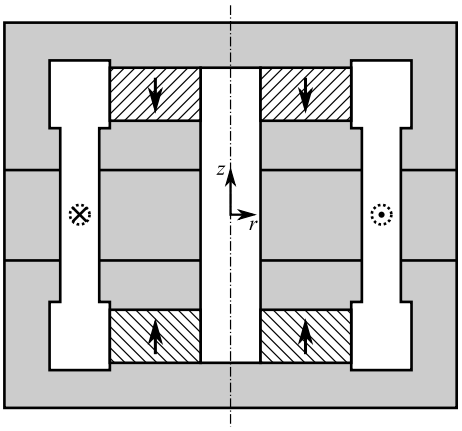

Fig. 1. Drawing of the magnet system. The hatched areas are the permanent magnets with the magnetization directions indicated by the arrows. The gray areas represent the soft iron yoke. This geometry was used originally by the BIPM and has been copied by various laboratories around the world, including NIST. The assembly is similar to the NIST-4 magnet [2], and the yoke is composed of six parts of soft steel.

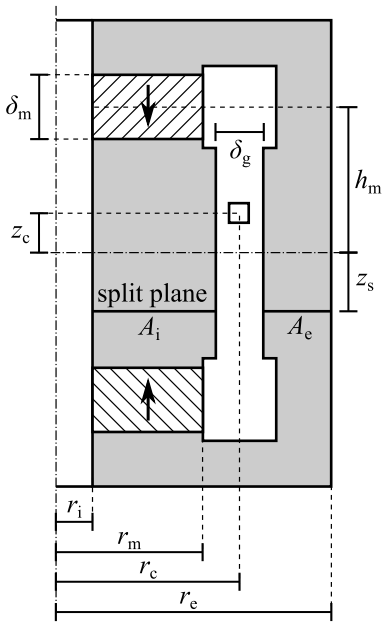

Fig. 2. Dimensions of the magnet system used for the analytical models. There are nine main geometrical parameters present in the models described here.

yoke, yokeless permanent magnets, and hybrid magnets that combine any of these options. There are advantages and disadvantages to these possibilities for generating B. The permanent magnets represent an option with relative simple design and operation while having low cost and maintenance. There are different designs for magnet systems based on permanent magnets used in the Kibble balances [4]. The design pioneered by the International Bureau of Weights and Measures (BIPM) is the most frequently used and is employed by several laboratories around the world, including the BIPM itself and the national metrology institutes in China [5], Germany [6], South Korea [7], Switzerland [8], Turkey [9], and United States [2]. Fig. 1 shows a drawing of the magnet system, which is based on the NIST-4 Kibble balance. Due to several advantages of the BIPM design, this option was chosen for the QEMMS Kibble balance. This design provides good shielding due to the closed yoke and has great past performance in previous versions of the Kibble balances. This magnet system was used during high-precision measurements of the Planck constant that occurred before the redefinition of the SI [10]. The main drawback of the design is that the magnet must be split apart to install, access, or repair the coil. For the NIST-4 magnet, the force required to split the magnet is about 4.7 kN. Such a large force makes the splitting process difficult, and a dedicated magnet splitter was necessary [3]. The large mass of the NIST-4 magnet system of about 850 kg makes the manipulation of the magnet system even more complicated.

Both the disadvantages, i.e., a heavy magnet and the need for a dedicated splitter, were addressed in the design for the QEMMS magnet. As a result, the discussed magnet weighs only 110 kg and can be split by applying a reasonable force of 250 N. The latter allows the integration of the magnet splitter into the magnet design, eliminating the need for a dedicated device. Similar to the magnet in the NIST-4, mounting fixtures will be bolted on the upper part of the magnet. As shown in Fig. 2, the lower third of the magnet can be removed. To further simplify the split process, the magnet system was designed such that the weight of the lower third matches the split force. Hence, it is not necessary to generate any additional force during the split process.

Several aspects must be considered designing a magnet system [2], [3], [11]–[13]: 1) the back action of the current on the magnetic flux density; 2) the flatness of the flux density profile; 3) the temperature dependence; and 4) the geometrical requirements of the balance, i.e., coil radius and length of the flat region. To design a magnet system that fulfills all requirements, it is necessary to evaluate several aspects using analytic models and simulations. The analysis is described in Section III.

III. Performance Evaluation

Five aspects of the magnet system are evaluated: 1) the magnetic circuit; 2) the reluctance force on the coil; 3) the force required to split the magnet; 4) the flatness of the flux density in the air gap as a function of vertical position, i.e., the field profile; and 5) the required size, the wire gauge, and the number of turns for the coil. For this evaluation, the dimensions shown in Fig. 2 were used and are summarized as follows: width of the air gap $\delta_g = 2.6$ cm, height of each permanent magnet $\delta_m = 3.5$ cm, distance of the center of the permanent magnet from the symmetry plane $h_m = 8$ cm, location of the split plane relative to the symmetry plane $z_s = 3$ cm, radius of the internal bore $r_i = 2$ cm, radius of the permanent magnet $r_m = 8$ cm, radius of the coil $r_c = 10$ cm, and outer radius of the complete system $r_e = 15$ cm. The active magnetic components of the magnet system are two composite, identical rings made from TC-16 ($Sm_2Co_{17}Gd$) arc segments. Alloying Gd together with SmCo reduces the remanence temperature coefficient of the magnet to $-0.001\%/K$. The price to pay for the temperature compensation is a reduced

remanence of $Sm_2Co_{17}Gd$ compared to that of Sm_2Co_{17}. For the material used, the remanence is B_r of 0.83 T.

A. Magnetic Circuit

The magnetic circuit equation is used to estimate the magnetic flux density in the air gap. In Appendix A, a derivation of the magnetic flux Φ through the coil based on the magnetic circuit is provided. The product Bl and the magnetic flux are related by the following expression:

$$Bl = N\frac{d\Phi}{dz_c}(I = 0). \tag{1}$$

By combining (1) and (30) and considering the fact that $l = 2\pi r_c N$, the following expression for the magnetic flux density B in the air gap can be obtained:

$$B = \frac{B_r}{2r_c h_m/\left(r_m^2 - r_i^2\right) + \mu_m \delta_g/\delta_m} \tag{2}$$

where $\mu_m = 1.06$ is the relative permeability of the magnetic material. Using 2, the magnetic flux density in the air gap is estimated to be 240 mT. The finite-element analysis (FEA) yields a value of approximately 245 mT. The same calculations were performed for the NIST-4 magnet system. The results from the analytical model and simulation are 525 mT and 554 mT, respectively. Measurements published in [3] indicate a value of 553 mT for the radial flux density. Hence, there is a good agreement between model, simulation, and measurement. The analytical model represents a simple way to determine the magnetic flux in the air gap as a function of the parameters of the magnet system.

For the determination of the magnet circuit equation, it was assumed that the yoke material has a high permeability. Soft steel classified by the American Iron and Steel Institute (AISI) as 1010 is considered for the yoke, and permeability of 2700 is expected. This material offers a high permeability at a reasonable cost. Fig. 3 shows the radial flux density in the air gap as a function of the yoke permeability. Fig. 3 is a simulation result obtained with FEA. A significant variation in the flux density can be observed for a relative permeability smaller than 1000. For higher values of permeability, the variation of the flux density in the air gap is very small. The magnet system is designed such that the iron is not magnetically saturated at any point in the magnetic circuit, and variations in the permeability do not affect much the flux density in the air gap.

B. Reluctance Force

The reluctance force is caused by a position-dependent variation of the magnetic flux through the coil when an electric current is flowing. This problem has already been considered in [2], [12], and [13]. A similar analysis is performed here. In this analysis, the magnetic flux in both the air gap and permanent magnet are considered to determine the reluctance force.

This force can be determined by using the following expression [14]:

$$F_r = -\frac{\partial E_c}{\partial z_c} \tag{3}$$

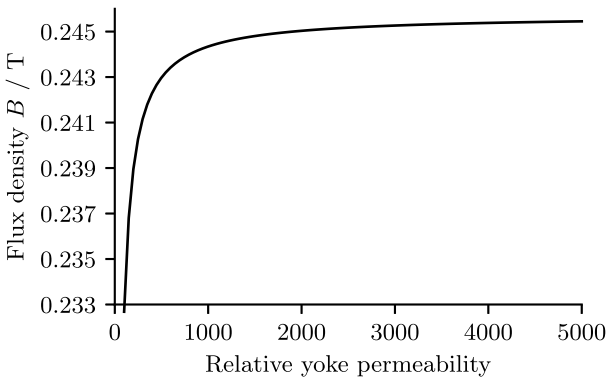

Fig. 3. Radial flux density in the air gap as a function of the yoke permeability. The expected relative permeability of the material to be used is 2700.

where E_c is the energy stored in the coil. It can be obtained by integrating the coil power $P_c = dE_c/dt = u_c I$, where the coil voltage is determined by using Faraday's law of induction

$$u_c = -N\frac{d\Phi}{dt} = -N\frac{\partial\Phi}{\partial I}\frac{dI}{dt}. \tag{4}$$

The energy stored in the magnetic flux caused by the coil current is given by

$$E_c = \int dE_c = -N\int I\frac{\partial\Phi}{\partial I}dI = -\frac{NI^2}{2}\frac{\partial\Phi}{\partial I}. \tag{5}$$

By combining (3), (5), and (30), the following expression for the reluctance force can be obtained:

$$F_r = -\frac{\pi\mu_0 N^2 r_c z_c I^2/\delta_g}{h_m + \mu_m\delta_g\left(r_m^2 - r_i^2\right)/(2r_c\delta_m)}. \tag{6}$$

The reluctance force can also be described relative to the nominal force generated by the coil, which is equal to $F = BlI$. The relative reluctance force is defined as $f_r = F_r/F$ and is given by

$$f_r = -\frac{\mu_0 r_c N I z_c}{\delta_g B_r\left(r_m^2 - r_i^2\right)}. \tag{7}$$

For a given magnetic material, the relative reluctance force can be reduced by increasing the air gap width δ_g or the radius of the magnetic material r_m. By reducing the number of turns N, the coil radius r_c, the internal hole radius r_i, or the coil current I, the relative reluctance force can also be reduced. The ratio between the relative reluctance force and the coil position multiplied by the current $(z_c I)$ gives a constant value that can be used to quantify the influence of the reluctance force. The reluctance force constant is defined as

$$c_{rf} = \frac{f_r}{z_c I}. \tag{8}$$

In order to avoid measurement deviations, it is important to minimize this quantity. The magnet system of the QEMMS Kibble balance gives a c_{rf} of approximately $-4.51\,m^{-1}A^{-1}$. A value of $-4.45\,m^{-1}A^{-1}$ was obtained by performing an FEA. For these calculations, a Bl of 700 Tm was used. The reluctance force constant was also determined for the NIST-4 magnet system, resulting in $-0.237\,m^{-1}A^{-1}$ and

$-0.235\,\mathrm{m}^{-1}\mathrm{A}^{-1}$ for the model and FEA, respectively. Reference [3] contains a measurement result of the second derivative of the coil inductance with respect to vertical position. The value $\partial^2 L/\partial z_c^2 = -346\ \mathrm{H/m}^2$ can be converted to the reluctance force constant and yields $-0.244\ \mathrm{m}^{-1}\mathrm{A}^{-1}$. This conversion can be performed by using $Bl = 709$ Tm and

$$c_{\mathrm{rf}} = \frac{1}{2Bl}\frac{\partial^2 L}{\partial z_c^2}. \tag{9}$$

Equation (9) here agrees better with simulation and measurement than previously published equations in [2] and [13]. The improvement stems from the fact that, here, the entire magnetic flux through the coil is considered for the determination of the reluctance force and not just the magnetic flux through the air gap.

In the Kibble balance experiments, the weighing process is normally performed in a way to eliminate measurement deviations caused by the reluctance force. For this, the weighing process is divided in two phases, named, mass-on and mass-off. For the first phase, the measuring mass m is placed on the weighing pan, and for the second phase, the same mass is removed. The following equations can be obtained for both phases:

$$BlI_{\mathrm{ON}}(1 + c_{\mathrm{rf}} z_c I_{\mathrm{ON}}) = mg - m_t g \tag{10}$$

$$BlI_{\mathrm{OFF}}(1 + c_{\mathrm{rf}} z_c I_{\mathrm{OFF}}) = -m_t g. \tag{11}$$

The tare mass m_t represents an imbalance added to the balance counterweight. It is adjusted such that the weighing currents have equal magnitude and opposite directions

$$I_{\mathrm{ON}} = -I_{\mathrm{OFF}} = \Delta I. \tag{12}$$

By subtracting (11) from (10) and using (12), the following expression is obtained:

$$m = \frac{2\Delta I Bl}{g}. \tag{13}$$

In theory, the component related to the reluctance force drops out and is not present in (13). However, to obtain this result, it was assumed that the coil position z_c is the same for both mass-on and mass-off phases. This is not the case in practice [10], and for this reason, it is important to minimize the reluctance force constant c_{rf} during the design of the magnet system.

C. Force Required to Split the Magnet

Appendix B contains the derivation of an analytical equation to calculate the force required to split the magnet as a function of the vertical position of the split plane. The final equation is obtained by combining (33)–(34), yielding

$$F_z = \frac{\pi r_c B^2}{\mu_0}\left(\frac{2\pi r_c (A_i + A_e)}{A_i A_e} z_s^2 - \delta_g\right) \tag{14}$$

where A_i and A_e are the areas of the yoke in the split plane, as indicated in Fig. 2. They are given in (36) and (37), respectively.

Fig. 4 shows a comparison between (14) and a simulation for the QEMMS Kibble balance magnet system. There is a good agreement between the model and simulation results. For a split plane in the middle ($z_s = 0$), a repulsive force of about 400 N is present. Choosing the location of the split plane at $z_s = 2.4$ cm results in the zero split force. For higher split plane heights, the force becomes repulsive and increases. By analyzing this plot and considering that the split plane should fall outside the precision air gap with a height of ± 2 cm, the location of the split plane was chosen to be at $z_s = 3$ cm. For this height, the force required to open the magnet system is 250 N. The mass of the lower third of the magnet system is estimated to be 28 kg. When suspended from the top, the weight of the lower third is equal and opposite to the split force, simplifying the split operation. Since the additional force that is required to open the magnet is close to zero, the magnet splitter can be integrated into the magnet design instead of building a dedicated device.

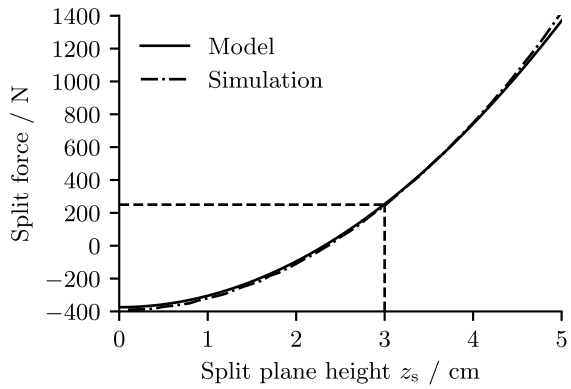

Fig. 4. Model and simulation result for split force as a function of the split plane height. For the simulation, FEA was used. Negative represents force in repulsive direction and positive represents force in attractive direction.

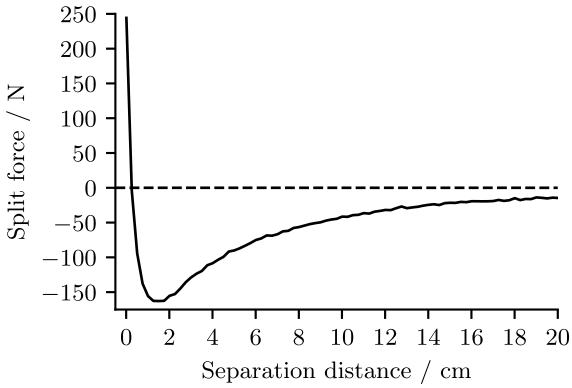

Fig. 5. Simulation result for the split force as a function of the separation between the magnets. This is a result of FEA. Negative represents force in the repulsive direction, and positive represents force in the attractive direction.

Fig. 5 shows a simulation result for the force on either magnet part as a function of separation for a split plane height of $z_s = 3$ cm. The initial force is attractive with a magnitude of 250 N. At a distance of 0.25 cm, the force reverses sign and becomes repulsive. The largest repulsive force with a magnitude of about 160 N is observed for a distance between 1 cm and 2 cm. For larger distances, the force converges to 0 N.

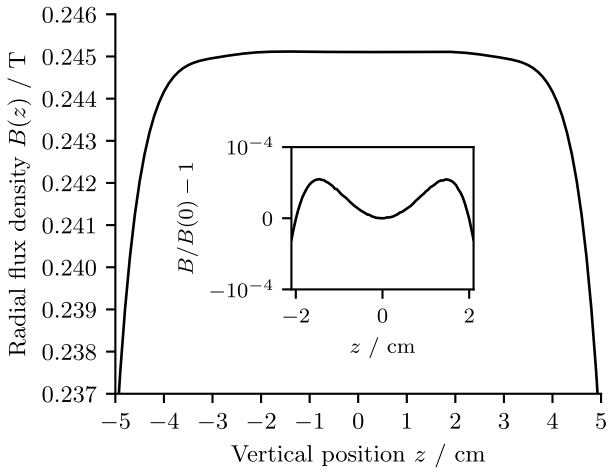

Fig. 6. Profile for the radial magnetic flux density B. The box inside the plot shows the profile deviation for the precision air gap of 4 cm. This profile was obtained by using FEA.

D. Profile of the Magnetic Field

The functional dependence of the radial magnetic flux density on the vertical position is commonly known as the profile of the magnetic field. It can be determined by using FEA. Fig. 6 shows an FEA result. The magnetic flux density stays relatively within a band of $\pm 6 \times 10^{-5}$ in a region of ± 4 cm about the symmetry plane. For the QEMMS Kibble balance, stability better than 1×10^{-4} is required. It is possible to decrease the fluctuation of the profile within the ± 4 cm, by increasing the height h_{m} as observed with FEA. The disadvantage would be a taller and heavier magnet. Since the flatness of the profile is already better than is required, this option was not pursued. Increasing the height h_{m} above the optimal height, the flatness of the field will decrease.

The profile flatness has been considered in previous publications [2], [3], [13], [15]. Because of the importance of a stable B profile, there are several methods available for optimizing and shimming the magnet system. Due to the complexity of the problem, it is not simple to obtain an analytical solution. For this reason, most of the publications are based on simulation and measurement results.

E. Coil Parameters

It is necessary to determine the number of turns and the diameter of the current-carrying coil used with the permanent magnet system. For a given radial magnetic flux density, the length of the wire will determine Bl. As described in [2], this product can be chosen in a way to minimize the uncertainty for the mass measurement. This is done by considering the single uncertainties for the measurements of electrical resistance, voltage, velocity, and acceleration of free fall, together with the uncertainty equation for the mass measurement

$$\frac{\sigma_{\mathrm{m}}^2}{m^2} = \frac{\sigma_{U_{\mathrm{R}}}^2 B^2 l^2}{R^2 m^2 g^2} + \frac{\sigma_{\mathrm{R}}^2}{R^2} + \frac{\sigma_{\mathrm{g}}^2}{g^2} + \frac{\sigma_{\mathrm{v}}^2}{v^2} + \frac{\sigma_{\mathrm{U}}^2}{B^2 l^2 v^2}. \tag{15}$$

By using the expected uncertainties with this equation, it is possible to obtain the relative uncertainty for the mass measurement as a function of the parameter Bl. A plot with this relation is shown in Fig. 7. The velocity v is expected to be measured with a relative uncertainty of 8×10^{-9} for a constant value of about 2 mm/s. A resistance R of 1 kΩ will be used for the current measurement, and the resistance value is expected to be known with a relative uncertainty of 6×10^{-9} . The acceleration of free fall g is measured with a relative uncertainty of 5×10^{-9} , and the voltages U_{r} and U are measured with an uncertainty of 1 nV. The relative uncertainty for the mass measurement was determined for a mass m of 100 g. A flat region with minimal uncertainties is present for a Bl between 400 Tm and 1000 Tm. A value of 700 Tm is chosen for the QEMMS magnet system. For a radial flux density of 0.24 T and a coil radius of 10 cm, about 4642 turns are necessary to reach this Bl.

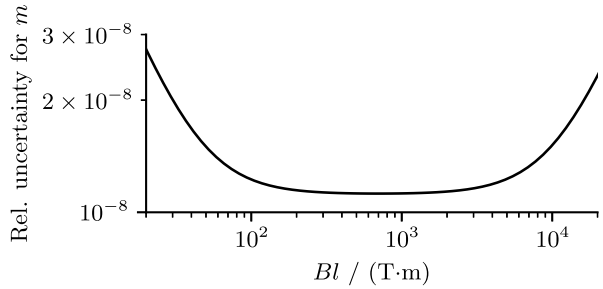

Fig. 7. Determination of the Bl value using the same procedure described in [2]. There is a flat region with minimum values between 400 and 1000 Tm.

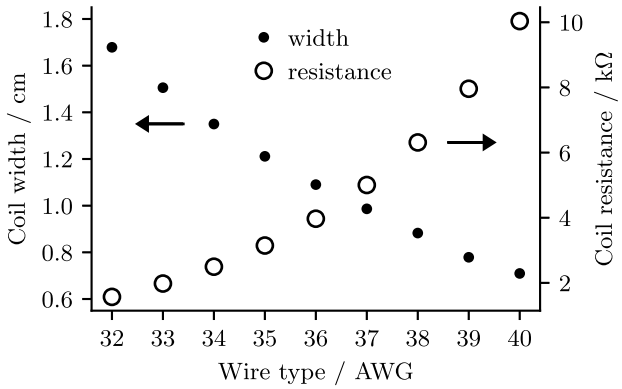

Fig. 8. Coil side length and resistance as a function of the wire gauge. A square coil cross section was used for the calculations.

Once the length of the wire, i.e., the number of turns, is determined, the wire diameter must be chosen. Two competing factors must be weighed against each other. Using a wire with a larger diameter yields a lower resistance for the coil, and hence, the less power dissipation and, therefore, a smaller temperature increase when switching from velocity mode to weighing mode. On the other hand, winding the coil with a wire that has a larger diameter increases the size and weight of the coil. The width of the air gap limits the size of the coil in one direction, and plenty of clearance between the former and the iron of the yoke should be taken into consideration to avoid collisions of the coil with the yoke by parasitic motions. The coil width and resistance as a function of the wire type are shown in Fig. 8. For the results shown in Fig. 8, a square cross section for the coil was assumed, round magnet wires with

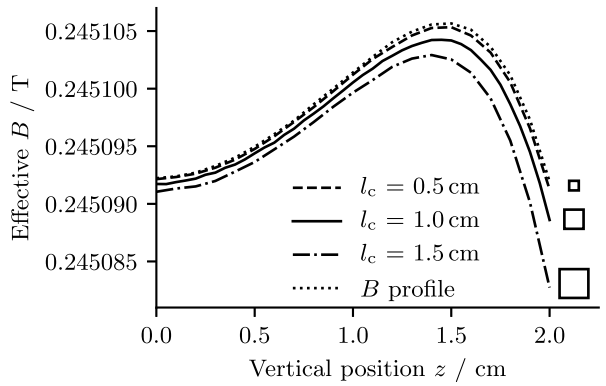

Fig. 9. Simulation results for the determination of the B profile for different coil side lengths. A square coil cross section was used for the simulations. The coil cross section is shown on the right-hand side.

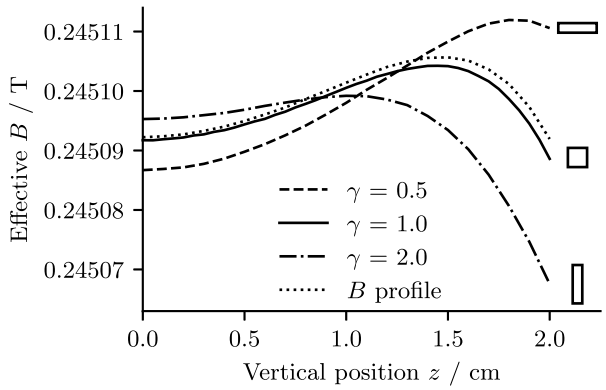

Fig. 10. Influence of the aspect ratio in the B profile. For these simulation results, a coil with cross section area of 1 cm^2 was used. The coil cross section is shown on the right-hand side.

double insulation layer were considered [16], and a packing factor of 0.785 for the winding was assumed. It should be noted that a packing factor of up to 0.86 can be achieved [17] for the wire types shown in Fig. 8. Hence, the calculation is conservative.

Since the coil has a finite size, the effective profile seen by the coil is an integration of the magnetic flux density over the coil volume. Fig. 9 compares the effective profile of three square coils with different sizes to the original profile. The curves shown in Fig. 9 were obtained with FEA, and the mean radius of the radius r_c was the same for all calculations. For all three cases, the effective profile is attenuated from the original profile. The larger the square coil, the smaller the effective field. The relative difference between the effective profiles and the original profile, however, is smaller than 4×10^{-5} in all three cases.

Fig. 10 shows the influence of the coil aspect ratio in the flux density profile as observed by the coil. For these simulation results, a coil with cross section area of 1 cm^2 was used. The height and width are given as $(A_c)^{1/2} \cdot \gamma$ and $(A_c)^{1/2}/\gamma$, respectively, where A_c represents the cross section area and γ the aspect ratio. As shown in Fig. 10, a higher aspect ratio represents a flatter flux density profile near to the center of the magnet system. However, in this case, the deviations are bigger for positions far from the center. For aspect ratios smaller than one, the flatness of the flux density profile in the center is compromised, and the overall deviations in the profile are higher. Aspect ratios equal to one or slightly higher seem the best choices for the Kibble balance application. In NIST-4, for example, an aspect ratio of 1.12 was chosen. For the QEMMS Kibble balance, an aspect ratio of one will be used. The coil will be wound using AWG 36 wires with double insulation leading to a coil resistance of 4 kΩ. In force mode, the coil will dissipate 2.1 mW, which is less than half of the power dissipation in the NIST-4. A coil side length of about 1.1 cm, which is shown in Fig. 8, represents enough space in the air gap to mount a coil form and operate the balance.

IV. Proposed Design of the QEMMS Magnet

The values of the key parameters of the QEMMS magnet system and coil are shown in Table I. For comparison, the corresponding values of NIST-4 are also shown. The major difference between both balances is the measuring range: QEMMS is being designed to measure masses up to 100 g with relative uncertainties lower than 2×10^{-8} , while NIST-4 can measure masses up to 2 kg, but nominally operates at 1 kg. QEMMS is intended to be smaller than NIST-4 and easier to operate. Hence, a smaller magnet system that is about eight times lighter than that of NIST-4 will be used. The split forces are much smaller, and an integrated magnet splitter will be used to separate the magnet system *in situ* and access the coil. TC-16 will be used as the active magnetic material resulting in better temperature stability for the remanence B_r than the samarium cobalt used in NIST-4. The tradeoff for a lower temperature coefficient is a lower remanence, which reduces the flux density in the air gap. A smaller travel range equal to 4 cm is required for the QEMMS, and a smaller coil with half of the size of the coil employed in NIST-4 will be used. The coil in QEMMS has five times more turns than the coil in NIST-4, and hence, a smaller wire gauge is necessary. As a consequence, the resistance and inductance of the QEMMS coil are larger than the corresponding values in the NIST-4 coil. However, due to the smaller nominal mass in QEMMS (100 g versus 1 kg), the thermal power generated in the coil is smaller for QEMMS. Also, the reluctance force does not yield a significant contribution to the measurement uncertainty. Although the reluctance force constant is 19 times larger for the QEMMS, the smaller nominal mass means a factor of 1.9 in relative increase. In addition, the lower mass value causes a smaller deviation in the coil position between the mass-on and mass-off measurement phases described in Section III-B. This behavior also reduces the measurement deviations caused by the reluctance force.

V. Summary

The design considerations and the final design of the magnet system driven by the basic requirements of the QEMMS were described in this article. The new magnet system is based on the NIST-4 magnet, and it was designed to take advantage of the past performance of NIST-4 while overcoming known practical limitations such as the large temperature coefficient. Analytical models for describing the magnetic flux density

TABLE I
COMPARISON BETWEEN THE MAGNET SYSTEMS AND COILS FOR THE QEMMS AND THE NIST-4

	QEMMS	NIST-4
Design goals for the balance		
Nominal mass value	100 g	1 kg
Relative uncertainty	2×10^{-8}	1×10^{-8}
Parameters of the magnet system		
Flux density B	0.24 T	0.55 T
Precision air gap	4 cm	8 cm
Magnetic material	TC-16	Sm_2Co_{17}
Mass of magnet	110 kg	850 kg
Split force	250 N	4.7 kN
Parameters of the coil		
Mean radius	10 cm	21.7 cm
Aspect ratio	1	1.12
Cross sectional area	$1\,cm^2$	$2.64\,cm^2$
Number of Turns	4642	945
Wire size	AWG 36	AWG 24
Resistance	4 kΩ	108 Ω
Properties of the coil in the magnet		
Inductance	33.9 H	4.06 H
Heating power	2.1 mW	5.5 mW
Reluct. force const.	$-4.51\,m^{-1}\,A^{-1}$	$-0.237\,m^{-1}\,A^{-1}$

in the air gap, the reluctance force in the coil, and the split forces for the separation operation are given in this article. With these models and FEA, the performance of the magnet system was evaluated. Aspects related to the coil geometry and flatness of the flux density profile were also considered. The proposed design will be manufactured and tested to verify that the magnet meets its operational requirements.

APPENDIX A
EQUATIONS FOR THE MAGNETIC CIRCUIT

The equivalent magnet circuit for the magnet system of Fig. 2 is shown in Fig. 11. There are two permanent magnets in the system: the top and bottom magnets. The yoke and the air gap are also divided into two parts named top and bottom. The magnetic flux through the top yoke and top magnet is named Φ_{tm}, and the magnetic flux through the air gap is named Φ_{tg}. For the lower part, the magnet fluxes Φ_{bm} and Φ_{bg} are defined. The magnetic flux through the coil is given by Φ. The following relationship can be obtained for the magnetic fluxes by applying the Gauss law of magnetism to two separate closed surfaces S_T and S_B comprising the nodes above and below the coil, respectively:

$$\Phi = \Phi_{tm} - \Phi_{tg} = \Phi_{bg} - \Phi_{bm}. \tag{16}$$

By using the Ampere circuital law, the following equations can be obtained for the parts of the magnet circuit indicated with the numbers 1–3, respectively:

$$H_{ty}\delta_y + H_{tg}\delta_g - H_{tm}\delta_m = 0 \tag{17}$$

$$H_{bg}\delta_g - H_{tg}\delta_g = NI \tag{18}$$

$$H_{by}\delta_y + H_{bg}\delta_g - H_{bm}\delta_m = 0 \tag{19}$$

where H_{ty} and H_{by} are the magnitude of the magnetic field in the top and bottom yokes, H_{tg} and H_{bg} are the magnitude

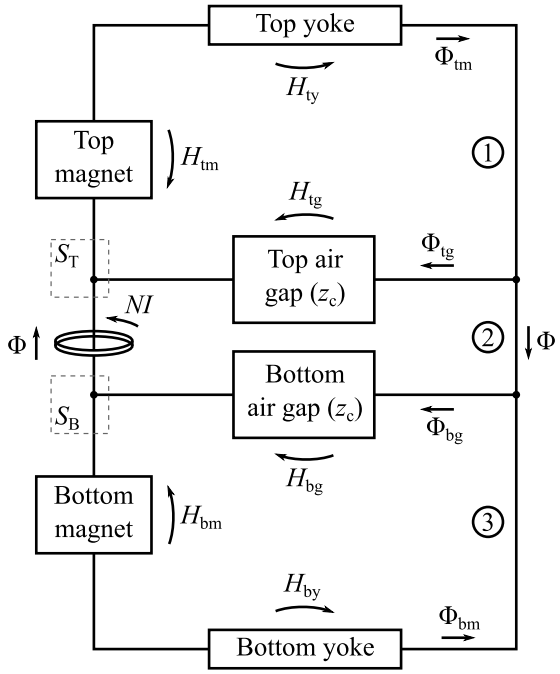

Fig. 11. Drawing of the magnetic circuit used to obtain the equations for the system. Top and bottom air gaps depend on the coil position z_c.

of the magnetic field in both parts of the air gap, and H_{tm} and H_{bm} are the magnitude of the magnetic field in the permanent magnets. The quantities δ_g and δ_m are the width of the air gap and the height of the permanent magnets, respectively. The effective length of the yoke is defined by δ_y. It is known that the magnetic field is a vectorial field, and inside the different components of the magnet system, there is a significant variation of this quantity over the space. To obtain the above-mentioned equations, it is necessary to assume that the magnetic field has a constant magnitude for the yoke, the permanent magnets, and the air gap. The quantities that represent the magnitude of the magnetic field can be seen as a mean value along the integration path.

Since the yoke is made of a ferromagnetic material, the following expressions are obtained for the magnetic flux densities as a function of the magnetic field:

$$B_{ty} = \mu_y H_{ty}, \quad B_{by} = \mu_y H_{by} \tag{20}$$

where the quantity μ_y represents the yoke permeability. A linear magnetization curve was assumed for the yoke material.

The permanent magnets are made of rare earth materials, and the magnetization curves are also assumed to have a linear behavior

$$B_{tm} = B_r - \mu_0\mu_m H_{tm}, \quad B_{bm} = B_r - \mu_0\mu_m H_{bm} \tag{21}$$

where B_r represents the remanence and μ_m the recoil permeability.

The flux density in both parts of the air gap is given by the following expressions:

$$B_{tg} = \mu_0 H_{tg}, \quad B_{bg} = \mu_0 H_{bg}. \tag{22}$$

By assuming that the magnet flux density has a constant magnitude inside the yoke, air gap, and permanent magnets, the following expressions can be obtained for the magnetic fluxes:

$$\Phi_{\mathrm{tm}} = B_{\mathrm{ty}} A_{\mathrm{y}} = B_{\mathrm{tm}} A_{\mathrm{m}} \tag{23}$$

$$\Phi_{\mathrm{bm}} = B_{\mathrm{by}} A_{\mathrm{y}} = B_{\mathrm{bm}} A_{\mathrm{m}} \tag{24}$$

$$\Phi_{\mathrm{tg}} = B_{\mathrm{tg}} A_{\mathrm{tg}} \tag{25}$$

$$\Phi_{\mathrm{bg}} = B_{\mathrm{bg}} A_{\mathrm{bg}} \tag{26}$$

where A_{y} is the effective area of the yoke. The area of the permanent magnets is given by

$$A_{\mathrm{m}} = \pi \left(r_{\mathrm{m}}^2 - r_{\mathrm{i}}^2\right) \tag{27}$$

and the areas of the top and bottom parts of the air gap are given by

$$A_{\mathrm{tg}} = 2\pi r_{\mathrm{c}} (h_{\mathrm{m}} - z_{\mathrm{c}}) \tag{28}$$

$$A_{\mathrm{bg}} = 2\pi r_{\mathrm{c}} (h_{\mathrm{m}} + z_{\mathrm{c}}). \tag{29}$$

By combining the expressions above and neglecting the magnetic field in the yoke, the following expression can be obtained for the magnetic flux through the coil:

$$\begin{aligned}\Phi = {} & \frac{NI\mu_0}{2\delta_{\mathrm{g}}}\left(2\pi r_{\mathrm{c}} h_{\mathrm{m}} + \mu_{\mathrm{m}}\pi\left(r_{\mathrm{m}}^2 - r_{\mathrm{i}}^2\right)\delta_{\mathrm{g}}/\delta_{\mathrm{m}}\right) \\ & + \frac{2\pi r_{\mathrm{c}} z_{\mathrm{c}} B_{\mathrm{r}}}{2r_{\mathrm{c}} h_{\mathrm{m}}/\left(r_{\mathrm{m}}^2 - r_{\mathrm{i}}^2\right) + \mu_{\mathrm{m}}\delta_{\mathrm{g}}/\delta_{\mathrm{m}}} \\ & - \frac{\pi r_{\mathrm{c}} N I z_{\mathrm{c}}^2 \mu_0/\delta_{\mathrm{g}}}{h_{\mathrm{m}} + \mu_{\mathrm{m}}\left(r_{\mathrm{m}}^2 - r_{\mathrm{i}}^2\right)\delta_{\mathrm{g}}/\left(2r_{\mathrm{c}}\delta_{\mathrm{m}}\right)}.\end{aligned} \tag{30}$$

The magnetic field in the yoke can be neglected due to the relative high permeability of the yoke material. This equation has basically three components that are related to the coil inductance in the center of the magnet system, the Bl factor, and the reluctance force, respectively.

The approach used in this appendix to determine the flux density through the coil is similar to methods used in [2], [11], [18], and [19].

Appendix B
Equation for the Split Force

The determination of the split force is necessary to design the magnet system in a way to integrate a simple magnet splitter. This force can be determined by integrating the Maxwell stress tensor $\boldsymbol{T}$ along the surface S indicated in Fig. 12

$$\boldsymbol{F} = \oiint_{\mathrm{s}} \boldsymbol{T} \cdot \mathrm{d}\boldsymbol{a} \tag{31}$$

where the Maxwell stress tensor is given by

$$T_{ij} = \frac{1}{\mu_0}\left(B_i B_j - \frac{1}{2}\delta_{ij} B_{\mathrm{m}}^2\right). \tag{32}$$

These equations were obtained by assuming static behavior and the absence of electric fields. The separation between both parts of the magnet system is assumed to be very small. A derivation for this equation is described with details in [20]. In the original derivation, a Cartesian coordinate system was used, and B_i or B_j represents the magnet flux densities along the different directions. That means i and j can be equal to the directions x, y, and z. The quantity B_{m} represents the magnitude of the flux density, and δ_{ij} is the Kronecker delta. For cylindrical coordinates, the following equation can be obtained:

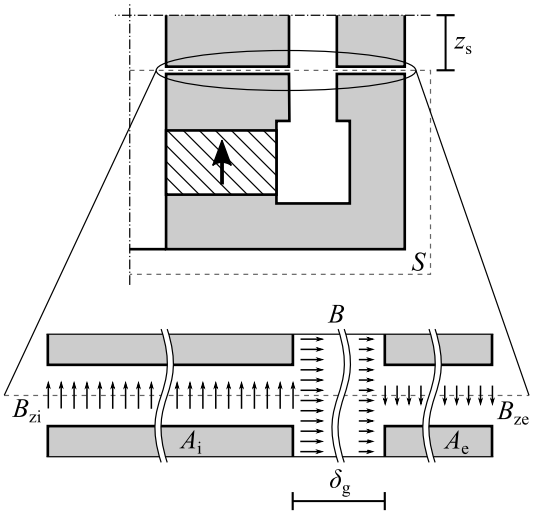

Fig. 12. Magnet system and surface area S used for integration of the Maxwell stress tensor and determination of the split force.

$$F_{\mathrm{z}} = \frac{1}{2\mu_0}\left(B_{\mathrm{ze}}^2\ A_{\mathrm{e}} + B_{\mathrm{zi}}^2 A_{\mathrm{i}} - 2\pi r_{\mathrm{c}} B^2 \delta_{\mathrm{g}}\right) \tag{33}$$

where B_{ze} and B_{zi} are the magnetic flux densities shown in Fig. 12. Due to the symmetry of the problem, for the split plane in the middle, which means $z_{\mathrm{s}} = 0$, the flux densities B_{ze} and B_{zi} are equal to 0. The flux density is horizontal in the air gap and vertical in the split plane. The flux densities B_{ze} and B_{zi} are proportional to the height of the split plane z_{s} and B

$$B_{\mathrm{ze}} = 2\pi r_{\mathrm{c}} z_{\mathrm{s}} B / A_{\mathrm{e}} \tag{34}$$

$$B_{\mathrm{zi}} = 2\pi r_{\mathrm{c}} z_{\mathrm{s}} B / A_{\mathrm{i}} \tag{35}$$

with the areas A_{i} and A_{e} given as

$$A_{\mathrm{i}} = \pi (r_{\mathrm{c}} - \delta_{\mathrm{g}}/2)^2 - \pi r_{\mathrm{i}}^2 \tag{36}$$

$$A_{\mathrm{e}} = \pi r_{\mathrm{e}}^2 - \pi (r_{\mathrm{c}} + \delta_{\mathrm{g}}/2)^2. \tag{37}$$

In order to obtain these equations, it was assumed that the magnetic flux density outside the separation region is near to zero. A combination of (33)–(34) gives the following expression for determination of the split force:

$$F_{\mathrm{z}} = \frac{\pi r_{\mathrm{c}} B^2}{\mu_0}\left(\frac{2\pi r_{\mathrm{c}}(A_{\mathrm{i}} + A_{\mathrm{e}})}{A_{\mathrm{i}} A_{\mathrm{e}}} z_{\mathrm{s}}^2 - \delta_{\mathrm{g}}\right). \tag{38}$$

References

[1] M. Stock, R. Davis, E. de Mirandés, and M. J. T. Milton, "The revision of the SI—The result of three decades of progress in metrology," *Metrologia*, vol. 56, no. 2, Feb. 2019, Art. no. 022001.

[2] S. Schlamminger, "Design of the permanent-magnet system for NIST-4," *IEEE Trans. Instrum. Meas.*, vol. 62, no. 6, pp. 1524–1530, Jun. 2013.

[3] F. Seifert *et al.*, "Construction, measurement, shimming, and performance of the NIST-4 magnet system," *IEEE Trans. Instrum. Meas.*, vol. 63, no. 12, pp. 3027–3038, Dec. 2014.

[4] I. A. Robinson and S. Schlamminger, "The watt or Kibble balance: A technique for implementing the new SI definition of the unit of mass," *Metrologia*, vol. 53, no. 5, pp. A46–A74, Sep. 2016.
[5] Z. Li *et al.*, "The improvements of the NIM-2 joule balance," *IEEE Trans. Instrum. Meas.*, vol. 68, no. 6, pp. 2208–2214, Jun. 2019.
[6] C. Rothleitner *et al.*, "The Planck-Balance—Using a fixed value of the Planck constant to calibrate E1/E2-weights," *Meas. Sci. Technol.*, vol. 29, no. 7, May 2018, Art. no. 074003.
[7] M. Kim *et al.*, "Establishment of KRISS watt balance system to have high uniformity performance," *Int. J. Precis. Eng. Manuf.*, vol. 18, no. 7, pp. 945–953, Jul. 2017.
[8] D. Tommasini, H. Baumann, A. Eichenberger, and A. Vorotszhov, "The ultra-stable magnet of the Mark II experiment," *IEEE Trans. Appl. Supercond.*, vol. 26, no. 4, Jun. 2016, Art. no. 0602405.
[9] H. Ahmedov, N. B. Aşkın, B. Korutlu, and R. Orhan, "Preliminary Planck constant measurements via UME oscillating magnet Kibble balance," *Metrologia*, vol. 55, no. 3, pp. 326–333, Apr. 2018.
[10] D. Haddad *et al.*, "Measurement of the Planck constant at the National Institute of Standards and Technology from 2015 to 2017," *Metrologia*, vol. 54, no. 5, pp. 633–641, Jul. 2017.
[11] S. Li, Z. Zhang, and B. Han, "Nonlinear magnetic error evaluation of a two-mode watt balance experiment," *Metrologia*, vol. 50, no. 5, pp. 482–489, Sep. 2013.
[12] S. Li, F. Bielsa, M. Stock, A. Kiss, and H. Fang, "Coil-current effect in Kibble balances: Analysis, measurement, and optimization," *Metrologia*, vol. 55, no. 1, pp. 75–83, Dec. 2018.
[13] S. Li, F. Bielsa, M. Stock, A. Kiss, and H. Fang, "A permanent magnet system for Kibble balances," *Metrologia*, vol. 54, no. 5, pp. 775–783, Sep. 2017.
[14] J. L. Kirtley, "6.007 electromagnetic energy: From motors to lasers supplemental class notes energy method for finding forces," Massachusetts Inst. Technol., Cambridge, MA, USA, Tech. Rep., Sep. 2010.
[15] Q. You, J. Xu, Z. Li, and S. Li, "Designing model and optimization of the permanent magnet for joule balance NIM-2," *IEEE Trans. Instrum. Meas.*, vol. 66, no. 6, pp. 1289–1296, Jun. 2017.
[16] *Copper Magnet Wire Data*, MWS Wire Ind., Westlake Village, CA, USA, Sep. 2016.
[17] C. W. T. McLyman, *Transformer and Inductor Design Handbook*, 3rd ed. Boca Raton, FL, USA: CRC Press, 2004.
[18] S. Li, M. Stock, and S. Schlamminger, "A new magnet design for future Kibble balances," *Metrologia*, vol. 55, no. 3, pp. 319–325, Apr. 2018.
[19] H. A. Leupold and E. Potenziani, "A permanent magnet circuit design primer," U.S. Army Res. Lab., Fort Monmouth, NJ, USA, Tech. Rep. ARL-TR-946, Jul. 1996.
[20] D. J. Griffiths, *Introduction to Electrodynamics*, 3rd ed. Upper Saddle River, NJ, USA: Prentice-Hall, 1999.

Rafael R. Marangoni was born in Porto Alegre, Brazil. He received the Diploma degree in mechatronics from the University of São Paulo, São Paulo, Brazil, in 2014, the M.Sc. degree in electrical engineering from the Technical University of Darmstadt, Darmstadt, Germany, in 2014, and the Dr.Ing. degree in mechanical engineering from the Technical University of Ilmenau, Ilmenau, Germany, in 2019.

Since 2019, he has been a Post-Doctoral Fellow with the National Institute of Standards and Technology, Gaithersburg, MD, USA. He is currently involved in the research on the Kibble balance.

Darine Haddad (M'09) received the Ph.D. degree in optics, optoelectronics, and microwaves from the University of Versailles, Versailles, France, in 2004.

She was with the University of Versailles, where she was involved in teaching and conducting research in the field of optical sensors and dimensional metrology. She was a Post-Doctoral Fellow with the Laboratoire National de Metrologie et d'Essais, Trappes, France, in 2004, and the National Institute of Standards and Technology, Gaithersburg, MD, USA, in 2008, where she was involved in the Kibble balance experiments to measure the Planck constant and realizing mass.

Frank Seifert was born in Berlin, Germany. He received the Dipl.Ing. and Dr.Ing. degrees in electrical engineering from the Leibniz University of Hannover, Hannover, Germany, in 2002 and 2009, respectively.

From 2009 to 2012, he was with the California Institute of Technology, Pasadena, CA, USA, where he was involved in the research on the frequency stabilization of lasers for high-precision metrology. He is currently with the National Institute of Standards and Technology, Gaithersburg, MD, USA, and also with the Joint Quantum Institute, University of Maryland at College Park, College Park, MD, USA, where he is involved in the research on the Kibble balance.

Leon S. Chao received the B.S. degree in mechanical engineering from the University of Maryland at College Park, College Park, MD, USA, in 2012, where he is currently pursuing the Graduate degree.

In 2012, he joined the Fundamental Electrical Measurements Group, National Institute of Standards and Technology, Gaithersburg, MD, as a Mechanical Engineer, where he is currently involved in two Kibble balance experiments: NIST-4 and KIBB-g1.

David B. Newell received the Ph.D. degree in physics from the University of Colorado at Boulder, Boulder, CO, USA, in 1994.

He was a National Research Council Post-Doctoral Fellow with the National Institute of Standards and Technology (NIST), Gaithersburg, MD, USA, where he was involved in the Kibble Balance Project. In 1996, he was a Staff Member with NIST. From 2004 to 2010 and since 2018, he has been a Leader of the Fundamental Electrical Measurements Group, NIST. He was involved in measurements for the realization of microscale and nanoscale forces traceable to the International System of Units (SI), helped establish the use of graphene in quantum electrical standards and was involved in the construction of a new Kibble balance to realize the kilogram from a fixed value of the Planck constant.

Dr. Newell is also a member of the Philosophical Society of Washington and a fellow of the American Physical Society. He is also the Chair of the CODATA Task Group on Fundamental Constants, which provided the exact values of the fundamental constants that form the foundation of the revised SI.

Stephan Schlamminger (M'12) received the Diploma degree in physics from the University of Regensburg, Regensburg, Germany, in 1998, and the Ph.D. degree in experimental physics from the University of Zurich, Zürich, Switzerland, in 2002. His Ph.D. thesis was on the determination of the Universal Constant of Gravitation.

From 2002 to 2010, he was with the University of Washington, Seattle, WA, USA, where he was involved in the experimental test of the equivalence principle. In 2010, he was with the National Institute of Standards and Technology (NIST), Gaithersburg, MD, USA, where he was involved in the Kibble balance. In 2016, he was a Group Leader of the Fundamental Electrical Measurement Group, NIST. From 2017 to 2018, he was with the Regensburg University of Applied Science, Regensburg, where he taught physics. Since 2018, he has been a Physicist with NIST.